Spectral Modification of Shock Accelerated Ions Using a Hydrodynamically Shaped Gas Target

O. Tresca, N. P. Dover, N. Cook, C. Maharjan, M. N. Polyanskiy, Z. Najmudin, P. Shkolnikov, and I. Pogorelsky

Phys. Rev. Lett. **115**, 094802 — Published 28 August 2015

DOI: 10.1103/PhysRevLett.115.094802

Spectral modification of shock accelerated ions using a hydrodynamically shaped gas target

O. Tresca[1], N. P. Dover[2], N. Cook[3], C. Maharjan[3],
M. N. Polyanskiy[1], Z. Najmudin[2], P. Shkolnikov[2], and I. Pogorelsky[1]
[1] *Accelerator Test Facility, Brookhaven National Laboratory, Upton, New York 11973, USA*
[2] *John Adams Institute for Accelerator Science, Blackett Laboratory, Imperial College London, SW7 2BZ, United Kingdom and*
[3] *Stony Brook University, Stony Brook, New York 11794, USA*
(Dated: June 8, 2015)

We report on reproducible shock acceleration from irradiation of a $\lambda = 10\,\mu$m CO_2 laser on optically shaped H_2 and He gas targets. A low energy laser prepulse ($I \lesssim 10^{14}\,\mathrm{Wcm^{-2}}$) was used to drive a blast wave inside the gas target, creating a steepened, variable density gradient. This was followed, after 25 ns, by a high intensity laser pulse ($I > 10^{16}\,\mathrm{Wcm^{-2}}$) that produces an electrostatic collisionless shock. Upstream ions were accelerated for a narrow range of prepulse energies. For long density gradients ($\gtrsim 40\mu$m), broadband beams of He^+ and H^+ were routinely produced, whilst for shorter gradients ($\lesssim 20\mu$m), quasi-monoenergetic acceleration of protons was observed. These measurements indicate that the properties of the accelerating shock and the resultant ion energy distribution, in particular the production of narrow energy spread beams, is highly dependent on the plasma density profile. These findings are corroborated by 2D PIC simulations.

The light and thermal pressure associated with intense lasers causes compression and heating when incident on an overdense plasma. This can generate a piston that launches electrostatic collisionless shocks into the plasma [1]. Upstream ions reflected off the shock can create a population accelerated to twice the velocity of the driving shock [2–5]. This mechanism has been demonstrated in recent experiments using intense CO_2 lasers interacting with gas jets [6, 7] where multi-MeV proton beams with energy spread smaller than 4% have been reported.

Gas jets have also been proposed as a source of high purity high-Z ion beams. This is in contrast with the multiple species beams typically generated from solid targets [8, 9]. For solid targets, protons from surface contaminants are preferentially accelerated due to their higher charge-to-mass ratio, making the production of impurity free high-Z beams challenging. Generating, for example, high purity helium beams from gas jets would be of interest for nuclear and medical physics applications [10].

Laser driven [3, 11–13] acceleration of helium ions from laser irradiation of gas jets has been observed experimentally. However, these previous studies were conducted in underdense plasmas requiring laser intensities $> 10^{20}\,\mathrm{Wcm^{-2}}$. Collisionless shock acceleration, on the other hand, allows the production of directed beams at lower intensities with sizeable number [6], and with favourable intensity scaling [5].

It is thought that the generation and subsequent properties of shock accelerated ion beams are highly dependent on the initial plasma density distribution [5, 14]. In previous experiments using intense CO_2 lasers, it was surmised that the profile was modified by a pulse train inherent to the laser system [6, 7], which varied from shot-to-shot, making the interactions challenging to reproduce. Instabilities such as laser filamentation and hosing from the leading pulses result in variable density profiles, which in turn leads to fluctuation in the resultant ion beam. Recent breakthroughs in CO_2 laser technology have made single pulses of intense radiation possible [15]. This allows reproducible interaction of the laser with the target. However it requires a different method to modify the density profiles. One suggestion for achieving this is the use of optically generated hydrodynamic blast waves via laser solid interaction [16, 17].

In this paper, we demonstrate a novel method of hydrodynamically shaping gas targets to make them suitable for ion acceleration; through the production of a blast wave produced by a controlled low energy prepulse focused into the gas. Interaction of the high intensity laser pulse with the modified plasma density profile leads to reproducible shock acceleration. In particular, we present the first measurements of shock accelerated helium ions in a broad energy spread extending $> 1.5\,$MeV. Furthermore for the right laser and prepulse parameters, these beams can be produced with high reproducibility. With hydrogen, we can transition from broadband and quasi-monoenergetic ions beams depending once more on the prepulse energy and consequently the steepness of the initial front-surface plasma density gradient. PIC simulations confirm that the front surface scale-length is vital in controlling the properties of the accelerated ions.

The experiment was performed at the Accelerator Test Facility at the Brookhaven National Laboratory. A linearly polarized CO_2 laser beam, $\lambda = 10.3\,\mu$m, with energy up to 11 J per pulse of 5 ps (FWHM), provided a peak power of 2.2 TW. An $f/3$ parabolic mirror focussed the laser to a spot $w_0 = 65\,\mu$m, resulting in peak intensity $I = 2.5 \times 10^{16}\,\mathrm{Wcm^{-2}}$ ($a_0 = 1.4$). The laser was focussed at the center of a helium or hydrogen gas-jet from a 1 mm diameter supersonic nozzle, $\sim 700\,\mu$m

above the the nozzle. At this position the initial gas density profile, along the laser axis, was near triangular with a linear gradient of $\sim 1\,\mathrm{mm}$ up to a peak fully-ionized plasma density of $n_e \sim 2n_c$ [18]. The ion beam was characterized using an on-axis Thomson parabola spectrometer, opening angle of $2 \times 10^{-5}\,\mathrm{sr}$, and detected with BC-408 polyvinyl-toluene scintillator coupled to an EMCCD camera. The ion-to-detected-photon yield was calibrated using the Tandem proton accelerator at Stony Brook University [19]. The calibration was scaled to He^+ by introducing a scaling factor of 0.3 ± 0.1 [20].

A laser prepulse collinear to the drive pulse was generated to shape the gas. It arrived 25 ns before the main laser pulse and contained a variable energy, E_{pp}, up to 1 J in 5 ps. The resulting plasma density distribution was characterized using optical probing. Two, time-adjustable, $\sim 10\,\mathrm{ps}$ long, $\lambda = 532\,\mathrm{nm}$ synchronized pulses were used for shadowgraphy and interferometry. They were set to allow characterization just before and after the drive pulse on a single shot.

Fig. 1a shows the experimentally observed plasma density map 100 ps before the main laser plasma interaction (LPI) using He; similar images are found using H_2. For this shot, a prepulse $E_{pp} \approx 220\,\mathrm{mJ}$ was incident on gas of peak neutral density $n_{He} = 0.8 \times 10^{19}\,\mathrm{cm}^{-3}$, corresponding to a fully ionized plasma density $n_e = 1.6\,n_c$. n_e was obtained from interferometry assuming cylindrical symmetry around the laser axis, thus allowing Abel inversion. The optical path difference due to the unionized gas is small compared to that of the plasma and is therefore neglected. Plasma formation was observed over a large volume with a peak density significantly lower than the fully ionized density, and shows no structure. However, probing the plasma 300 ps after the LPI revealed the characteristic high density shell of a blast wave (fig. 1b). The shell is observed to expand at velocity $< 10^5\,\mathrm{ms}^{-1}$. Hence the dramatic change in the plasma appearance cannot be due to hydrodynamic motion originating from the main pulse interaction.

The effect of the prepulse was modelled using the FLASH hydrodynamics solver in 2D cylindrical geometry. He was initialized following the experimental gas jet profile with $n_{He} = 0.8 \times 10^{19}\,\mathrm{cm}^{-3}$. The prepulse energy was modelled by depositing thermal energy evenly into a cylinder of gas at the laser focus (length 600 μm and radius 80 μm) centered near the initial critical density surface; $n_{He} = \frac{1}{2}n_c$. Within 1 ns, a collisional blast wave is formed and expands out into the cold gas [21, 22]. The blast wave forms a cavity with low density but high electron temperatures at the center, surrounded by a cold but high density shock moving outwards. Fig. 1c shows the electron density at 25 ns after the prepulse, calculated from the Saha equation, for an initial 3 mJ of energy absorbed in the plasma. Only the center of the cavity is hot enough to be ionized and detectable by interferometry, in agreement with the experimental measurements

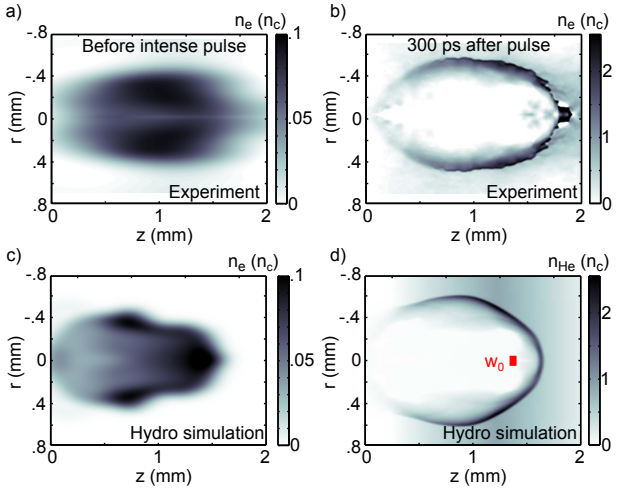

FIG. 1. Electron plasma density from He targets, n_e from interferometry: (a) immediately before, and (b) 300 ps after the LPI, for $E_{pp} \approx 220\,\mathrm{mJ}$. (c) n_e and (d) total helium atomic density (irrespective of ionization), n_{He} from hydro simulations after 25 ns of expansion for 3 mJ absorbed energy.

prior to the LPI in fig. 1a. Inspection of the neutral helium density (fig. 1d) reveals the blast wave, which has a cavity wall of peak density given by that of a strong shock $(\gamma+1)/(\gamma-1)n_i$, where n_i is the ion density and γ, the ratio of specific heats ($\frac{5}{3}$ for He, 1.4 for H_2) [21]. Therefore, using hydrogen with comparable laser parameters gives a higher density enhancement as well as a reduced scale length [23]. Even though this neutral profile exists

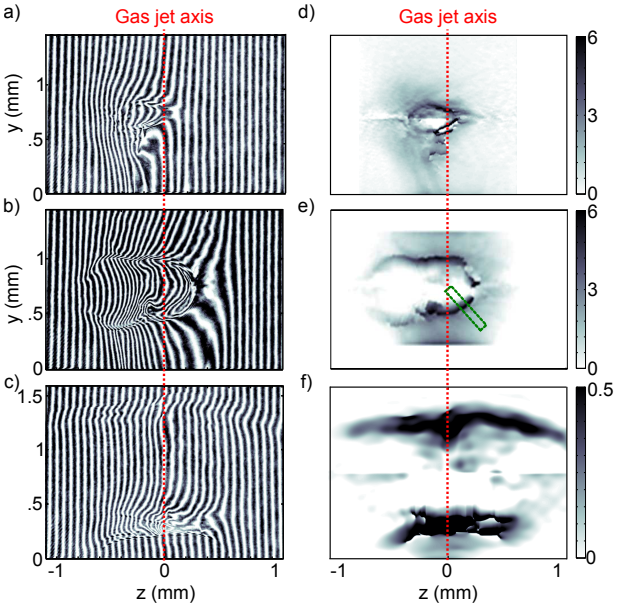

FIG. 2. Interferograms 300 ps after the LPI with He; (a) without prepulse, (b) with prepulse ideal for ion acceleration, $E_{pp} \approx 150\,\mathrm{mJ}$, (c) and with prepulse too large for ion acceleration, $E_{pp} \approx 1.27\,\mathrm{J}$. (d-f) corresponding n_e/n_{cr}.

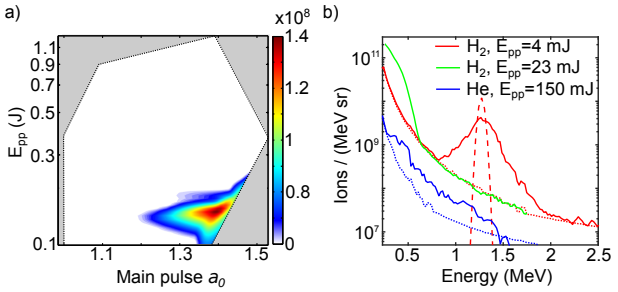

FIG. 3. (a) Average flux of accelerated helium ions (/sr) > 0.1 MeV as sampled by the spectrometer (color scale) as a function of prepulse energy, E_{pp} and main pulse a_0 The white region indicates laser parameters tested experimentally. (b) Proton spectra for a H_2 target with $E_{pp} \approx 4$ and 23 mJ, and He^+ spectrum for a He target with $E_{pp} \approx 150$ mJ (solid lines). The dotted lines are the detection thresholds, and the dashed red line is the deconvolved spectrum for $E_{pp} \approx 4$ mJ.

before the LPI, it is only due to ionization by the fast electrons generated during the main interaction that it can be directly observed. Once ionized, the blast wave provides a sufficiently high density plasma in which to generate collisionless shock waves.

Interferograms for three different prepulse levels with helium gas are shown in fig. 2a-c, with corresponding n_e in fig. 2d-f. The images are all taken 300 ps after the LPI to reveal the full blast wave structure. Similar images are obtained with H_2. To account for the vertical density gradient in the initial gas density, azimuthal symmetry is assumed in each half-cylinder above and below the laser axis. These regions were processed individually by Abel inversion, with continuity assumed at their interface.

With no prepulse (fig. 2a&d), a small cavity of diameter $\approx 100\,\mu$m forms around the laser focal position. The intense laser has self-focussed and channelled part way into the long density scale length ($l \approx 1$ mm), coupling most of the energy into the plasma ramp. In this case, no forward accelerated ions were observed.

Introducing a prepulse with energy $E_{pp} \approx 150$ mJ (fig. 2b&e) shows a significant difference in the plasma distribution. A blast wave was generated prior to the arrival of the intense pulse, so that the main pulse interacts with a profile with higher peak density and steeper gradient, rising from $n_e = 0$ to $\approx 6n_c$ in $\approx 100\,\mu$m. Energetic ions were consistently generated in this regime.

For further increase in E_{pp} (fig. 2c&f), the prepulse induced blast wave propagates deeper into the jet and ultimately through it, leaving only an underdense remnant along the laser axis. For this higher prepulse, no ion beam was observed. Probing in this case, showed little change to the shape of the plasma before and after the LPI, except for a doubling of the density in the walls, consistent with ionization from He^+ to He^{2+}.

Hence, control of the helium density profile generated by the blast wave is essential for reproducible ion acceleration. Fig. 3a shows the flux of detected He^+ ions (color scale) as a function of main pulse normalized vector potential, a_0, and prepulse energy, E_{pp}. The figure is generated from 36 shots from a single run with fixed focal position and density. Accelerated ions were only observed for six shots in a narrow range of prepulse energies, 110 mJ $\lesssim E_{pp} \lesssim$ 220 mJ, showing the importance of optimizing the density profile as in fig. 2b & d. Within this range of E_{pp} and $a_0 \approx 1.4$, the total flux of accelerated ions remains stable shot-to-shot at $\approx 10^8$ ions/sr ($\pm 3.10^7$ ions/sr).

Fig. 3b shows a He^+ spectra obtained with $E_{pp} = 150$ mJ and a main pulse $a_0 = 1.4$, resulting in a broad energy distribution up to 1.5 MeV. This spectrum was typical for all the observed beams. Only He^+ ions are observed although the main pulse laser intensity exceeds the threshold value to double ionize helium via field ionization ($I \gtrsim 9{\times}10^{15}$ Wcm^{-2}). The observed single charge state is the result of charge transfer as the ions traverse the plasma and un-ionized gas [12, 24], and recombination as the accelerated ion beam co-moves with a low temperature electron cloud to the detector.

For fixed n_i and absorbed energy E_{abs}, a blast wave in hydrogen will give a steeper density ramp than for helium due to the lower γ [23]. Spectra from shots with H_2 for different prepulse levels $E_{pp} = 4$ mJ and 23 mJ are also shown in fig. 3b. Note that a significantly smaller prepulse was required for ion generation with hydrogen; observation of the relative blast wave size implies a significantly higher energy absorption. For $E_{pp} = 4$ mJ, a quasi-monoenergetic beam is observed with peak energy ≈ 1.2 MeV and a deconvolved energy spread $\Delta E/E \approx 5\,\%$, compared with a broadband beam with energies up to ≈ 0.5 MeV for $E_{pp} = 23$ mJ. As the radius for a spherical blast-wave $r_{bw} \propto (E_{abs}/n_i)^{1/5}$ [21], lower E_{pp} results in less expansion, providing a steeper target density gradient. Hence, not only does this technique allow the production of reproducible shock accelerated ions, but spectral shaping is also achievable for sufficiently steep density gradients.

The use of a variable prepulse to steepen the target density profile differentiates this work from experiments where a prepulse incident on a solid target is used to generate low density targets through plasma expansion [25, 26]. Though this method can produce near-critical density targets of sufficient length for shock acceleration, they naturally produce targets with long density scale lengths, which as we demonstrate here, is not ideal for production of high quality beams.

The LPI was modelled using the 2D PIC code EPOCH. The plasma was initialized with 30 particles per cell of cold ions (He^{2+} or H^+) and electrons, in cells of size $\lambda/50$. The laser had $a_0 = 1.4$, $w_0 = 65\,\mu$m at focus, pulse length $\tau = 5$ ps (FWHM), and was linearly polarized in the transverse plane. The initial density distribution was varied to investigate the effect of the optical density tai-

loring. To model the LPI with no prepulse, the initial density profile was set to rise linearly from 0 to $2\,n_c$ over $800\,\mu$m with He^{2+}. The laser self-focuses and bores a channel in the plasma, shown in fig. 4a. All the laser energy is expended in the underdense region and no forward shock is formed, although lower velocity transverse electrostatic shocks are observed [3].

The effect of the prepulse was simulated using a plasma density distribution extracted from the interferometry for $E_{pp} \approx 150\,$mJ (green box in fig. 2b). The profile was taken along a line radially off-set from the laser axis in order to reduce errors introduced by the Abel inversion. In the blast-wave ramp the density is well approximated by $n = n_{max} e^{-(z_0-z)/l_{exp}}$, where $n_{max} \approx 6\,n_c$ is the peak density, z_0 is the position of the peak and $l_{exp} \approx 40\,\mu$m is the scale length. In this simulation, the laser pulse shows a modest increase in intensity due to self-focussing in the ramp, but the short ramp length means the laser is not adversely absorbed. The pulse penetrates up to the critical surface where a combination of radiation and thermal pressure launches a collisionless shock (fig. 4b). Ions are reflected at the shock front to twice the shock speed v_s. The result agrees well with optical shadowgraphy 300 ps after the LPI (inset of fig. 4b), which shows remnants of the accelerating collisionless shock emerging from the collisional prepulse induced blast wave.

The z-p_z phase space (fig. 4c) demonstrates that the ions originate from the position of the shock, but also that the ions are reflected with a large energy spread. Fig. 5a shows the position of the shock front and critical surface on the laser-axis as a function of time for this simulation. The initial shock velocity $v_{sh} \approx 5 \times 10^6\,\mathrm{ms}^{-1}$ exceeds the measured hole-boring velocity $v_{hb} = 3.1 \times 10^6 \approx \sqrt{I_L/n_i m_i c}$ [27, 28]. Ions reflected off the shock at its peak velocity would gain ~ 3.1 MeV, in agreement with simulated maximum ion energies of ~ 3.3 MeV (fig. 5b). The shock slows at the end of the laser drive while still reflecting ions, resulting in the large momentum spread in fig. 4b and the corresponding broadband axial ion spectrum in fig. 5b. The shock deceleration is mainly due to spherical expansion of the front. Scaling the simulated ion spectra to the experimental spectra and imposing the experimental detection limit as in fig. 3b results in a maximum detectable ion energy of ~ 2 MeV, consistent with that measured.

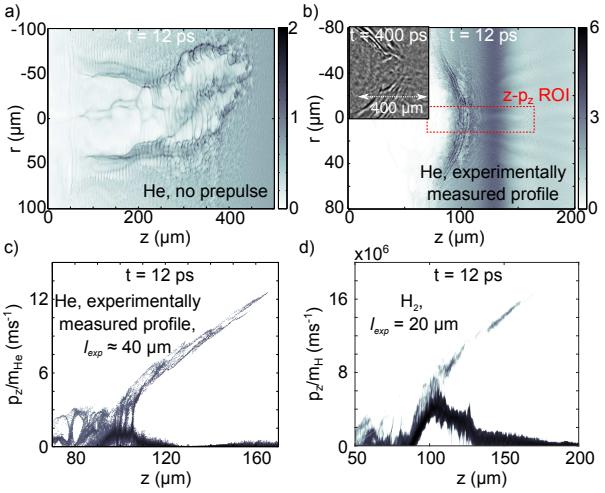

FIG. 4. Results of PIC simulations. Ion density map 12 ps after LPI for: (a) no prepulse, (b) experimental initial profile for $E_{pp} = 150\,$mJ obtained from fig. 2e. (inset is optical shadowgraphy showing shock remnants) and (c) z-p_z phase space. (d) The z-p_z phase space for for hydrogen plasma with exponential ramp ($l_{exp} = 20\,\mu$m)

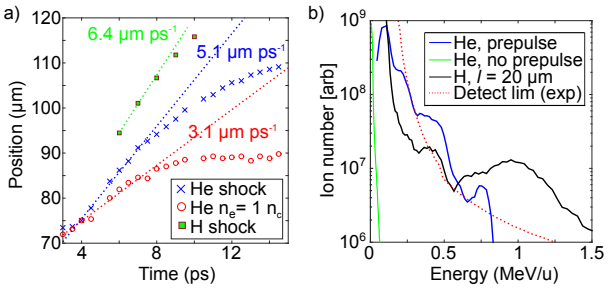

FIG. 5. (a) Critical surface (red) and shock (blue) position with time for He simulation shown in fig. 4b&c, and shock position for H simulation in fig. 4d. (b) Comparison of He^{2+} spectra for $800\,\mu$m linear ramp (no prepulse - green), He with $l_{exp} = 40\,\mu$m (prepulse - blue), and for H with $l_{exp} = 20\,\mu$m (black).

Simulations were also performed using the sharper density profiles achievable with H_2. In this case, a density drop to $\frac{1}{6}n_{max}$ at the edge of the blast-wave, as expected for a strong shock, imitated the experimental profile. A scale length $l_{exp} = 50\,\mu$m produces a broadband beam, as for helium. However, shortening the scale length to $l_{exp} = 20\,\mu$m results in the shock breaking through the density discontinuity at the blast-wave front. The sudden change in thermal pressure ahead of the front triggers immediate dissipation of the shock, just at the end of the LPI (fig. 5a). The axial z-p_z phase space, fig. 4d, demonstrates the formation of a single bunch with velocity near $2v_s \approx 13 \times 10^6\,$m/s. Particle reflection stops and the peaked spectrum is maintained (fig. 5d). This method of generating spectral peaks is thus quite different to maintaining a constant shock velocity over a longer time in an isothermal plasmas which requires the use of much longer laser pulses [5, 7]. Simulation with $l_{exp} < 10\,\mu$m with He also demonstrated spectrally peaked beams. Such gradients, though not possible in the present experimental set-up, could be achieved by shortening the time between the prepulse and the drive pulse.

In this work, we have shown that a steep initial front-surface plasma density scale length is crucial not only to achieve shock acceleration but also spectral control of the ion beam. It was observed that long density gradi-

ents hydrogen plasmas lead to the production of broad-band shock accelerated beams, while steeper gradients allow for the generation of quasi-monoenergetic beams. He ions have also been accelerated using this scheme, demonstrating that it could be extended to other high Z gaseous species, providing a route towards a wide variety of easily replenishable high-repetition rate ion sources for nuclear physics applications.

Work supported by the US DOE Grant DE-FG02-07ER41488, and UK EPSRC grant EP/K022415/1. FLASH was developed by the DOE NNSA ASC and NSF-supported FCCS at the U. Chicago. EPOCH development was supported by EPSRC grants EP/G054940/1, EP/G055165/1 and EP/G056803/1. Computing resources provided by Imperial College HPC services and NERSC (mp1401), supported by DOE Contract DE-AC02-05CH11231 and BNL/LDRD No. 12-032.

[1] J. Denavit, Phys. Rev. Lett., **69**, 3052 (1992).
[2] L. O. Silva et al., Phys. Rev. Lett., **92**, 015002 (2004).
[3] M. Wei, et al., Phys. Rev. Lett., **93**, 155003 (2004).
[4] L. M. Chen et al., Phys. Plasmas, **14**, 040703 (2007).
[5] F. Fiuza et al., Phys. Rev. Lett., **109**, 215001 (2012).
[6] C.A.J. Palmer et al., Phys. Rev. Lett., **106**, 014801 (2011).
[7] D. Haberberger et al., Nat. Phys., **8**, 95-99 (2012).
[8] E. L. Clark et al., Phys. Rev. Lett., **85**, 1654 (2000).
[9] R. Snavely et al., Phys. Rev. Lett., **85**, 2945 (2000).
[10] H. Daido et al. Rep. Prog. Phys. **75**, 056401 (2012).
[11] L. Willingale et al., Phys. Rev. Lett., **96**, 245002 (2006).
[12] F. Sylla et al., Phys. Rev. Lett., **108**, 115003 (2012).
[13] A. Lifschitz et al., New J. Phys., **16**, 033031 (2014).
[14] N. Dover et al., arXiv:1205.4558.
[15] M. N. Polyanskiy et al., Opt. Express, **19**, 7717 (2011).
[16] C. T. Hsieh et al., Phys. Rev. Lett. **96**, 095001 (2006).
[17] D. Kaganovich et al., Phys. Plasmas, **18**, 120701 (2011).
[18] Z. Najmudin et al., Phys. Plasmas, **18**, 056705 (2011).
[19] N. Cook, O. Tresca, and R. Lefferts, JINST, **9** 09004 (2014).
[20] G. Blasse and B.C. Grabmaier, *Luminescent Materials* (Springer, Berlin, 1994).
[21] Y. B. Zel'dovich and Y. P. Raizer, *Physics of Shock Waves and High-Temperature Hydrodynamic Phenomena* (Academic Press, New York, 1967).
[22] Yu. P. Raizer, Sov. Phys. Usp., **8** 650 (1966).
[23] L. I. Sedov, *Similarity and Dimensional Methods in Mechanics* (Academic Press, New York, 1959)
[24] A. Itoh, M. Asari and F. Fukuzawa, J. Phys. Soc. Jpn., **48**, 943 (1980); A. Itoh, K. Ohnishi and F. Fukuzawa, J. Phys. Soc. Jpn., **49**, 1513 (1980).
[25] M. Gauthier et al. Phys. Plasmas, **21**, 013102 (2015).
[26] H. Zhang et al. Phys. Plasmas, **22**, 013113 (2015).
[27] S. C. Wilks et al., Phys. Rev. Lett., **69**, 1383 (1992).
[28] A. P. L. Robinson et al. Plasma Phys. Control. Fusion, **51**, 024004 (2009).